The Astrophysical Journal, 935:97 (15pp), 2022 August 20 https://doi.org/10.3847/1538-4357/ac7de0

Gas and Cosmic-Ray Properties in the MBM 53, 54, and 55 Molecular Clouds and the Pegasus Loops Revealed by H I Line Profiles, Dust, and Gamma-Ray Data

T. Mizuno[1], K. Hayashi[2], J. Metzger[3], I. V. Moskalenko[4], E. Orlando[4,5,6], A. W. Strong[7], and H. Yamamoto[8]
[1] Hiroshima Astrophysical Science Center, Hiroshima University, Higashi-Hiroshima, Hiroshima 739-8526, Japan; mizuno@astro.hiroshima-u.ac.jp
[2] Institute of Space and Astronautical Science, Japan Aerospace Exploration Agency, 3-1-1 Yoshinodai, Chuo-ku, Sagamihara, Kanagawa 252-5210, Japan
[3] Department of Physics, The University of Chicago, Chicago, Illinois, 60637, USA
[4] W.W. Hansen Experimental Physics Laboratory, Kavli Institute for Particle Astrophysics and Cosmology, Stanford University, Stanford, CA, 94305, USA
[5] Department of Physics, University of Trieste and INFN, I-34127 Trieste, Italy
[6] Eureka Scientific, Oakland, CA, 94602-3017, USA
[7] Max-Planck Institut für extraterrestrische Physik, D-85748 Garching, Germany
[8] Department of Physics and Astrophysics, Nagoya University, Chikusa-ku Nagoya 464-8602, Japan
Received 2021 December 19; revised 2022 June 17; accepted 2022 June 30; published 2022 August 19

Abstract

In studying the interstellar medium (ISM) and Galactic cosmic rays (CRs), uncertainty of the interstellar gas density has always been an issue. To overcome this difficulty, we used a component decomposition of the 21 cm H I emission line and used the resulting gas maps in an analysis of γ-ray data obtained by the Fermi Large Area Telescope (LAT) for the MBM 53, 54, and 55 molecular clouds and the Pegasus loop. We decomposed the ISM gas into intermediate-velocity clouds, narrow-line and optically thick H I, broad-line and optically thin H I, CO-bright H_2, and CO-dark H_2 using detailed correlations with the H I line profiles from the HI4PI survey, the Planck dust-emission model, and the Fermi-LAT γ-ray data. We found the fractions of the optical depth correction to the H I column density and CO-dark H_2 to be nearly equal. We fitted the CR spectra directly measured at/near the Earth and the measured γ-ray emissivity spectrum simultaneously. We obtained a spectral break in the interstellar proton spectrum at $\sim$7 GeV, and found that the γ-ray emissivity normalization agrees with the AMS-02 proton spectrum within 10%, relaxing the tension with the CR spectra previously claimed.

Unified Astronomy Thesaurus concepts: Galactic cosmic rays (567); Gamma-rays (637); Interstellar medium (847)

1. Introduction

Interstellar space in the Milky Way is permeated with ordinary matter (gas or dust), which is known as the interstellar medium (ISM). It also contains high-energy charged particles known as cosmic rays (CRs), an interstellar radiation field (ISRF), and a magnetic field. These components are mutually interacting, and they play important roles in many physical and chemical processes (e.g., star formation). Hence, they have been studied in various wave bands from radio to γ-rays (for a review, see, e.g., Ferriere 2001).

Cosmic γ-ray emission (with photon energies $E \gtrsim 100$ MeV) is known to be a powerful probe for studying the ISM and Galactic CRs. High-energy CR protons and electrons interact with interstellar gas or the ISRF and produce γ-rays through nucleon–nucleon interactions, electron bremsstrahlung, and inverse-Compton (IC) scattering. Because the ISM is essentially transparent to those γ-rays (e.g., Moskalenko et al. 2006), we can study the ISM distribution via γ-ray observations. Because the γ-ray production cross section is independent of the chemical or thermodynamic state of the interstellar gas, cosmic γ-rays have been recognized as a unique tracer of the total column density of gas, regardless of its atomic or molecular state. If observations in other wave bands can be used to estimate the gas column density accurately, the CR spectrum and intensity distribution can be examined as well.

Usually, the distribution of neutral atomic hydrogen (H I) is measured directly via 21 cm line surveys (e.g., Dickey & Lockman 1990; Kalberla & Kerp 2009), assuming the optically thin approximation, and the distribution of molecular hydrogen (H_2) is estimated indirectly from carbon monoxide (CO) line-emission surveys (e.g., Dame et al. 2001), assuming a linear conversion factor. However, some fraction of the ISM gas in optically thick H I or CO-dark H_2 phases may be missed by these line surveys. Such "dark gas" can be studied using total gas tracers such as dust extinction, reddening, and emission (e.g., Reach et al. 1994) and γ-rays (e.g., Grenier et al. 2005). The work by Grenier et al. (2005) has been confirmed and improved by subsequent observations with the Fermi Large Area Telescope (LAT; Atwood et al. 2009). In addition, the Planck mission has provided an all-sky model of thermal emission from dust (Planck Collaboration XIX 2011; Planck Collaboration XI 2014) that is useful for the study of the ISM gas distribution because of its sensitivity and high angular resolution.

Despite these efforts, uncertainties in the ISM gas column density and the CR intensity are still uncomfortably large, by as much as a factor of $\sim$50% even in the local environment (see, e.g., Grenier et al. 2015). This is mainly due to the uncertainty in the spin–temperature (T_s) of H I gas, which affects the conversion from the 21 cm line intensity to the H I gas column density. To cope with this difficulty, some authors (e.g., Mizuno et al. 2016; Hayashi et al. 2019) have proposed to treat areas with high dust temperatures as optically thin H I and have used this assumption in analyzing Fermi-LAT γ-ray data. However, their method cannot distinguish gas phases along the line of sight, and hence, it is not applicable to the Galactic plane. Also, the composition of dark gas (i.e., the fractions of

optically thick H I and CO-dark H_2) is quite uncertain and is controversial. For example, while Fukui et al. (2015) proposed that optically thick H I dominates dark gas, Murray et al. (2018) claimed that dark gas is mainly molecular. Again, this is because the value of T_s is usually unknown, and neither dust nor γ-rays can distinguish between atomic and molecular gas phases.

H I absorption features (e.g., the optical depth profile) are often well represented by Gaussians, supporting the idea that gas motions within H I clouds have a random velocity distribution. H I emission profiles of most sources can also be decomposed into Gaussians, and components with narrow or broad line widths could be assumed to arise mainly from a cold neutral medium (CNM) or a warm neutral medium (WNM), respectively (e.g., Kalberla et al. 2020). Recently, Kalberla & Haud (2018) analyzed the all-sky HI4PI survey data (HI4PI Collaboration 2016) and decomposed the H I 21 cm line emission into Gaussian lines by taking account of spatial coherence. Although their analysis uses emission spectra only and hence suffers from systematic uncertainties in separating the CNM and WNM, it allows them to study H I line profies over the entire sky. Subsequently, Kalberla et al. (2020) found that narrow-line H I gas is associated with the dark gas estimated from infrared dust-emission maps by Schlegel et al. (1998). Specifically, H I lines with a Doppler temperature $T_D \leqslant 1000$ K (defined as $22 \times \delta_v^2$ where δ_v is the Gaussian line width in km s^{-1}) are associated with gas for which the column density is significantly larger than the optically thin case. Their work opens the possibility of identifying optically thin H I and dark gas using H I line profile information and hence decomposing the gas phases along the line of sight. We note that Kalberla et al. (2020) used H I emission data only to decompose narrow-line H I gas and attributed it to dark gas; hence, their results should be validated by an independent way. We also note that, although they interpreted the dark gas to be primarily CO-dark H_2, the thick H I hypothesis was not ruled out. To validate their work and establish a method applicable to the Galactic plane, we employed an H I-line-profile-based analysis to the MBM 53, 54, and 55 clouds and the Pegasus loop. They are nearby (100–150 pc) high-latitude clouds (Welty et al. 1989; Yamamoto et al. 2006) and hence are suitable for the detailed study of the ISM gas and CRs in the local environment. This region has been previously studied by Mizuno et al. (2016) using H I dust and γ-ray data but with a different method. Specifically, since Mizuno et al. (2016) modeled γ-ray data using dust maps as a tracer of the total gas column density, they could not distinguish optically thick H I and CO-dark H_2. Also, the gas-to-dust ratio was calibrated using a small area with a high dust temperature, and hence had a large uncertainty. We aim to overcome these difficulties by using H I line width information in this study.

This paper is organized as follows. We describe the properties of the ISM gas templates in Section 2, and the γ-ray observations, data selection, and modeling in Section 3. The results of the data analysis are presented in Section 4, where we confirm that narrow H I traces dark gas. We also find there remain residuals and employ a dust map to trace this residual gas. We interpret the narrow H I and residual gas templates as tracing different phases of the dark gas, and discuss the ISM properties in Section 5. We also compare the obtained γ-ray emissivity and CR spectra measured at/near the Earth and discuss the CR properties in Section 5. Finally, a summary of the study and future prospects are presented in Section 6.

2. ISM Gas Templates and Their Properties

We analyzed the γ-ray data in the region of Galactic longitude of $60° \leqslant l \leqslant 120°$ and Galactic latitude of $-60° \leqslant b \leqslant -28°$, which encompasses the MBM 53, 54, and 55 cloud complexes and the Pegasus loop. We prepared templates of the ISM gas for the γ-ray data analysis, as we did in Mizuno et al. (2016), but with updates, particularly for the atomic gas phase. Specifically, we prepared the following gas templates. All gas maps are stored in a HEALPix (Górski et al. 2005) equal-area sky map of order 9[9] with a mean distance of adjacent pixels of 6.′9 (0.114 deg) and a pixel size of 0.013 deg^2.

- $W_{H\,I}$ maps divided by H I line widths: we downloaded the H I line profile fits of Kalberla et al. (2020)[10] for our region of interest (ROI) and for peripheral regions ($\leqslant 5°$ from the boundaries). They modeled H I 21 cm emission of the HI4PI survey data (with an angular resolution of 16.′2 in FWHM in each sky direction using several Gaussians. And they gave the normalization, center, and width of each Gaussian component. As described by Kalberla & Haud (2018), they required the residuals to be consistent with the noise level, and also required the number of used Gaussians to be as low as possible by considering the information about the neighboring pixels. Negative normalizations or widths are given to suspicious lines (e.g., weak lines likely being artifacts due to the noise), and we discarded them when preparing the map. We then divide the H I data into three components: intermediate-velocity clouds (IVCs; e.g., Wakker 2001), with velocities outside the range -30 to $+20$ km s^{-1} (Fukui et al. 2014; Mizuno et al. 2016); H I clouds with narrow line widths ($T_D \leqslant 1000$ K. See Kalberla et al. (2020). Hereafter, we call them "narrow H I".); and those with broad line widths ($T_D \geqslant 1000$ K; hereafter called "broad H I"). The W_{HI} maps (maps of the integrated H I 21 cm line intensity) of these clouds are shown in Figure 1. Using the H I line profiles in map preparation is a major update over the work of Mizuno et al. (2016). In the narrow H I template, we can recognize coherent structures at around $l = 84°$ to 96° and $b = -44°$ to $-30°$ and an area of $\sim 20° \times 20°$ around $(l,\ b) \sim (109°,\ -45°)$. These features correspond to the MBM 53–55 clouds and the Pegasus loop, respectively.
- W_{CO} map: as we did in Mizuno et al. (2016), we used a W_{CO} map (map of the integrated ^{12}CO (J = 1–0) 2.6 mm line intensity) internally available to the LAT team. It combines the work by Dame et al. (2001) and new data at high Galactic latitudes. Those data were taken by two 1.2 m telescopes (one in the northern hemisphere and the other in the southern hemisphere) and smoothed to give an angular resolution of 18′ (FWHM) and sampled in 0.°25 intervals. The new CO data include most of the high-latitude CO clouds in the region studied here. As described by Dame (2011), the CO spectra are filtered and integrated over velocities to suppress noise. This map also is shown in Figure 1.

[9] This corresponds to a total number of pixels of $12 \times (2^9)^2 = 3145728$. (9 comes from the resolution index.)

[10] https://www.astro.uni-bonn.de/hisurvey/AllSky_gauss/

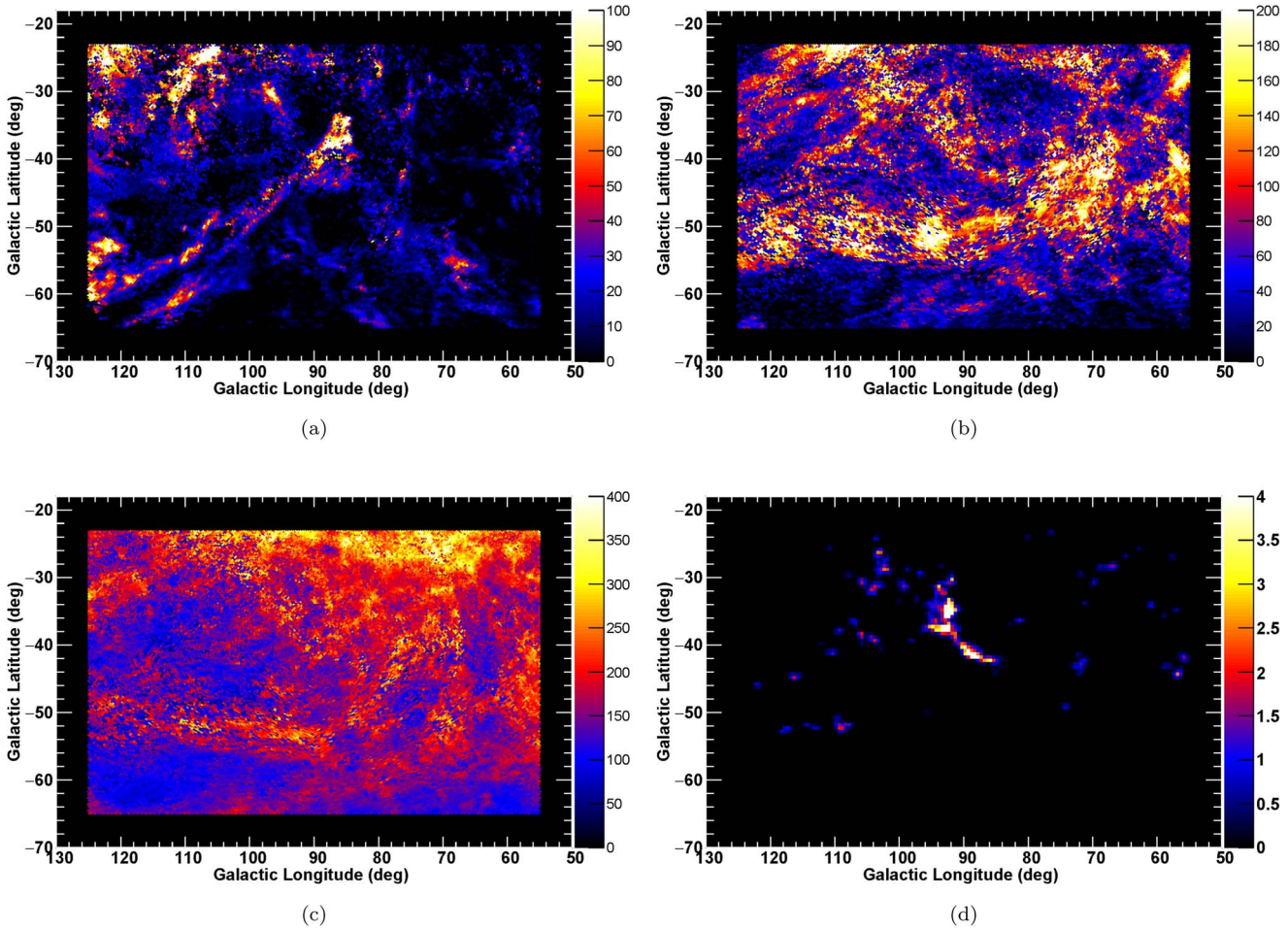

Figure 1. (a) $W_{\rm HI}$ map of the IVCs, (b) $W_{\rm HI}$ map of narrow H I, (c) $W_{\rm HI}$ map of broad H I, and (d) $W_{\rm CO}$ map. All these maps are shown in units of K km s^{-1}.

Planck dust-model maps: dust is a known tracer of the total gas column density, and it has been used to construct dark-gas templates for γ-ray data analysis (e.g., Abdo et al. 2010; Ackermann et al. 2011, 2012b). As we did in Mizuno et al. (2016), we used the Planck dust maps (of the radiance R, the opacity τ_{353} at 353 GHz, and the dust temperature $T_{\rm d}$) of the Public Data Release 1 (version R1.20)[11] described by the Planck Collaboration XI (2014). As reported by Mizuno et al. (2016), several areas have high $T_{\rm d}$, indicating localized heating by stars. To reduce their effects on the γ-ray data analysis, we refilled these areas (in the R, τ_{353}, and $T_{\rm d}$ maps) with the average of the peripheral pixels; see Appendix A for details. We also newly employed dust maps of the Planck Public Data Release 2 (version R2.00)[12] for comparison. We found that they are less affected by infrared sources, and we had to mask only one source using the same procedure. Both the Data Release 1 and 2 maps have an angular resolution of 5′ (FWHM). The R and $T_{\rm d}$ maps from Planck Data Release 1 are shown in Figure 2. We can recognize the MBM 53–55 clouds and the Pegasus loop in the R map. The τ_{353} map from Planck Data Release 1, and the R and τ_{353} maps from Planck Data Release 2 exhibit similar but different contrasts, and they predict different total gas column density distributions. We test them against the γ-ray data in Section 4.1.

3. Gamma-Ray Data and Modeling

3.1. Gamma-Ray Observations and Data Selection

LAT onboard Fermi Gamma-ray Space Telescope, which launched in 2008 June, is a pair-tracking γ-ray telescope that detects photons in the range from ∼20 MeV to more than 300 GeV. Details of the LAT instrument and the prelaunch performance expectations can be found in Atwood et al. (2009), and the on-orbit calibration is described by Abdo et al. (2009a). Thanks to its wide field of view (∼2.4 sr), Fermi-LAT is an ideal telescope to use for studying Galactic diffuse γ-rays. Although the angular resolution of γ-ray data is worse than those of gas tracers and is energy dependent (the 68% containment radiuses[13] are ∼5° and 0.°8 at 100 MeV and 1 GeV, respectively), it will be taken into account in the γ-ray data analysis described in Section 3.3. Past studies of Galactic diffuse emission by Fermi-LAT can be found in, e.g., Ackermann et al. (2012a) and Casandjian (2015).

Routine science operations with the LAT started on 2008 August 4. We have accumulated events from 2008 August 4 to 2020 August 3 (i.e., 12 yr) to study diffuse γ-rays in our ROI ($60° \leqslant l \leqslant 120°$ and $-60° \leqslant b \leqslant -28°$). During most of this

[11] https://irsa.ipac.caltech.edu/data/Planck/release_1/all-sky-maps/
[12] https://irsa.ipac.caltech.edu/data/Planck/release_2/all-sky-maps/
[13] Radius of a circle in which 68% of the photons from a source are contained

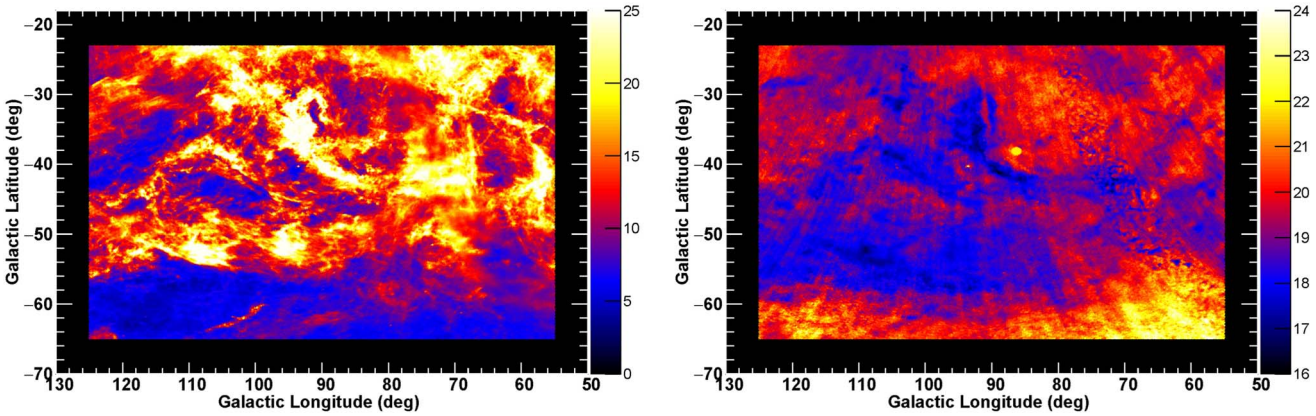

(a) (b)

Figure 2. (a) dust R map (10^{-8} W m^{-2} sr^{-1}) and (b) $T_{\rm d}$ map (K). Both maps are from Planck Data Release 1, and the infrared sources are masked as described in Appendix A.

time interval, the LAT was operated in sky-survey mode, obtaining complete sky coverage every two orbits (which corresponds to ∼3 hr), with relatively uniform exposures over time. We used the latest release of the Pass 8 (Atwood et al. 2013; Bruel et al. 2018) data (P8R3), which are less contaminated by a residual background than previous ones. We used the standard LAT analysis software, Fermitools[14] version 2.0.0, to select events satisfying the ULTRACLEAN class in order to obtain low-background events. We also required that the reconstructed zenith angles of the arrival directions of the photons be less than 100° and 90° for energies above and below 300 MeV, respectively, to reduce contamination by photons from Earth's atmosphere. To accommodate the relatively poor angular resolution at low energies, we used events and the responses of point-spread function (PSF) event types 2 and 3 below 300 MeV. However, above 300 MeV, we did not apply selections based on PSF event types to maximize the photon statistics. We used the `gtselect` command to apply the selections described above.

In addition, we referred to the Monitored Source List light curves,[15] and by using the `gtmktime` command, we excluded periods (∼1600 days in total) during which the LAT detected flares from 3C 454.3. This significantly reduced contamination in the diffuse emission from the bright active galactic nucleus. The count-rate threshold was more stringent than that used by Mizuno et al. (2016) in order to reduce the contamination better.[16] We also excluded periods during which the LAT detected bright γ-ray bursts or solar flares. (The integrated time excluded in this procedure is negligible compared to that excluded to remove data with flares from 3C 454.3.) Then we prepared a livetime cube by using the `gtltcube` command. We used the latest response functions that match our data set and event selection, P8R3_ULTRACLEAN_V3, in the following analysis.

As described in Section 3.2, we carried out a bin-by-bin likelihood fitting and took account of the energy dispersion. Using the latest P8R3 data, applying a tighter cut to the 3C454.3 flares, using PSF event types, and taking account of energy dispersion are major improvements in data selection and fitting, allowing us to lower the minimum energy used in the analysis down to 100 MeV.

3.2. Model to Represent Gamma-Ray Emission

We modeled the γ-ray emission observed by Fermi-LAT as a linear combination of the gas column density maps, IC emission, an isotropic component, and γ-ray point sources. The use of the gas column density maps as templates is based on the assumption that the γ-rays are generated via interactions between the CRs and ISM gas and that the CR intensities do not vary significantly over the scale of the interstellar complexes in this study. This assumption is simple but plausible, particularly in high Galactic latitude regions such as the one studied here, as has been verified by past studies of local clouds using Fermi-LAT data (for a review, see, e.g., Grenier et al. 2015). As described in Section 4, we started with three $N_{\rm H\,I}$ maps derived from the $W_{\rm HI}$ maps (assuming that the H I is optically thin) and a $W_{\rm CO}$ map (see Section 2). We then improved the templates by using the dust-emission ($D_{\rm em}$) model maps. We used the γ-ray emissivity model adopted by Abdo et al. (2009b) to calculate the γ-ray emissivity. To model the γ-rays produced via IC scattering, we used GALPROP[17] (e.g., Strong & Moskalenko 1998; Strong et al. 2007). GALPROP is a numerical code that solves the CR transport equation within the Galaxy and predicts the γ-ray emission produced via the interactions of CRs with interstellar matter and with low-energy photons (IC scattering). It calculates the IC emission from the distribution of propagated electrons and the ISFR. Specifically, we utilized the recent work by Porter et al. (2017). After testing several IC models against the γ-ray data with our baseline gas model (three $N_{\rm H\,I}+W_{\rm CO}$ templates), we decided to use an IC model based on a conventional CR distribution and the ISRF (SAO-Std model in Porter et al. 2017); see Appendix B for details. To model the individual γ-ray point sources, we referred to the fourth Fermi-LAT catalog (4FGL) described by Abdollahi et al. (2020), which is based on the first 8 yr of the science phase of the mission and includes more than 5000 sources detected at a significance level of $\geqslant 4\sigma$. For our analysis, we considered 128 4FGL sources (detected at a significance level $\geqslant 5\sigma$) in our ROI. In addition, we included

[14] https://fermi.gsfc.nasa.gov/ssc/data/analysis/software/

[15] https://fermi.gsfc.nasa.gov/ssc/data/access/lat/msl_lc/

[16] The lists of the mission elapsed time (the number of seconds since 2001 January 1) that passed the criteria are 2.45–2.72, 3.23–4.17, 5.05–5.45, and larger than 5.47 in 10^8.

[17] http://galprop.stanford.edu

bright sources ($\geqslant 20\sigma$) just outside it (within 10°), with the parameters fixed at those in the 4FGL, to consider their possible contamination. We also added an isotropic component to represent extragalactic diffuse emission and the residual instrumental background from misclassified CR interactions in the LAT detector. We adopted the isotropic template provided by the Fermi Science Support Center.[18]

Then, the γ-ray intensities $I_\gamma(l, b, E)$ (ph s^{-1} cm^{-2} sr^{-1} MeV^{-1}) can be modeled as

$$I_\gamma(l, b, E) = \Bigg[\sum_i C_{\mathrm{H\,I},i}(E) \cdot N_{\mathrm{H\,I},i}(l, b) + C_{\mathrm{CO}}(E) \cdot 2X^0_{\mathrm{CO}} \cdot W_{\mathrm{CO}}(l, b) + C_{\mathrm{dust}}(E) \cdot X^0_{\mathrm{dust}} \cdot D_{\mathrm{em}}(l, b)\Bigg] \cdot q_\gamma(E) + C_{\mathrm{IC}}(E) \cdot I_{\mathrm{IC}}(l, b, E) + C_{\mathrm{iso}}(E) \cdot I_{\mathrm{iso}}(E) + \sum_j \mathrm{PS}_j(l, b, E), \quad (1)$$

where the $N_{\mathrm{H\,I},i}$ is the atomic gas column density (cm^{-2}) model maps, q_γ (ph s^{-1} sr^{-1} MeV^{-1}) is the model of the differential γ-ray yield or γ-ray emissivity per H atom, W_{CO} is the integrated ^{12}CO ($J = 1$–0) intensity map (K km s^{-1}), and D_{em} is the dust-emission model (R or τ_{353}), which is a tracer of the total gas column density (see Section 4.1) or the residual gas (see Section 4.2). R and τ_{353} are given in W m^{-2} sr^{-1} and optical depth, respectively. The quantities I_{IC} and I_{iso} are the IC model and the isotropic template intensities (ph s^{-1} cm^{-2} sr^{-1} MeV^{-1}), respectively, and PS_j represents the point-source contributions. The subscript i allows for the use of $N_{\mathrm{H\,I}}$ maps from separate H I line profiles. We adopted the γ-ray emissivity model used by Abdo et al. (2009b). To accommodate the uncertainties, in either the emissivity model or the gas templates, we included normalization factors [$C_{\mathrm{H\,I},i}$, C_{CO}, or C_{dust} in Equation (1)] as free parameters. The quantities X^0_{CO} and X^0_{dust} are constant scale factors used to make the fitting coefficients (C_{CO} and C_{dust}) close to 1. Specifically, we use 1×10^{20} cm^{-2} (K km s^{-1})$^{-1}$ and 1.82×10^{28} cm^{-2} (W m^{-2} sr^{-1})$^{-1}$ for X^0_{CO} and X^0_{dust} (for R), respectively. While $C_{\mathrm{H\,I},i}$ will be 1 if $N_{\mathrm{H\,I},i}$ represents the true gas column density and the γ-ray emissivity agrees with the adopted model, C_{CO} and C_{dust} provide the CO-to-H_2 conversion factor ($X_{\mathrm{CO}} \equiv N_{\mathrm{H_2}}/W_{\mathrm{CO}}$, where $N_{\mathrm{H_2}}$ gives the molecular gas column density) and the dust-to-gas conversion factor, respectively. X_{CO} will be X^0_{CO} if $C_{\mathrm{H\,I},i}$ for optically thin H I ($C_{\mathrm{H\,I},3}$ will be described in Section 4.1) and C_{CO} are equal [$X_{\mathrm{CO}} = X^0_{\mathrm{CO}} \times (C_{\mathrm{CO}}/C_{\mathrm{H\,I},3})$]. The IC emission and isotropic models (see above) also are uncertain, and we have therefore included other normalization factors (the quantities C_{IC} and C_{iso} in Equation (1)) as free parameters. For the point sources, we adopted the spectral models in 4FGL; the spectral parameter of normalization was set to be free, and other spectral parameters and the positions of each source were fixed at the values in 4FGL. We divided the γ-ray data into several energy ranges and fitted Equation (1) to the γ-rays in each energy range using the binned-likelihood method, with energy dispersion taken into account, both implemented in Fermitools.

[18] https://fermi.gsfc.nasa.gov/ssc/data/access/lat/BackgroundModels.html

3.3. Model-fitting Procedure

We divided the γ-ray data into 10 energy bands extending from 0.1 to 72.9 GeV and stored them in HEALPix maps of order 8 (by using the `gtbin` command). We used a pixel size factor of 2 larger than those of the gas maps (Section 2) to accommodate for the small photon statistics, while keeping the γ-ray map fine enough to evaluate the gas distribution of H I. We used energy bins equally spaced logarithmically for the first eight bands (e.g., 0.1–0.17, 0.17–0.3, and 0.3–0.52 GeV) and employed bins twice as broad for the last two bands to accommodate for the small photon statistics. To evaluate the model's spectral shape, the data were subdivided into three (six) grids within the narrower (broader) energy bands. Then, in each energy band, we prepared exposure and source maps with finer grids taken into account (by using the `gtexpcube2` and `gtsrcmaps` commands), and fitted Equation (1) to the γ-ray data using the binned maximum-likelihood method with Poisson statistics implemented in Fermitools (by importing the `BinnedAnalysis` module in python). The angular resolution of the γ-ray data is taken into account in this step. Since the angular resolutions of the gas maps are much better than that of the γ-ray data in most of the energy range investigated, gas maps are convolved with the angular resolution of Fermi-LAT in the γ-ray data analysis. Also, since the statistical errors of the γ-ray data are much larger than the errors of the gas tracer intensity in most pixels, we do not take into account the latter when fitting the γ-ray data. We modeled $C_{\mathrm{H\,I},i}$, C_{CO}, C_{dust}, C_{IC}, and C_{iso} as energy-independent normalization factors in each energy band, and we modeled PS_j with only the normalization free to vary.

When modeling the point sources, we first sorted them (a total of 128 sources) by significance and divided them into 13 groups (each group has 10 sources at the maximum). We then iteratively fitted them in order of decreasing significance. First, we fitted the normalizations of the 10 most significant sources; then, we fitted the normalizations of the second group with parameters of the first group fixed at the values already determined. In this way, we worked down to the sources detected at more than 5σ in 4FGL. For each step, the parameters of the diffuse-emission model were always left free to vary. After we reached the least significant sources, we went back to the brightest ones and let them and the diffuse-emission models be free to vary while the parameters of the other sources were kept fixed at the values already determined. We repeated this process until the increments of the log-likelihoods, ln$L$,[19] were less than 0.1 over one loop in each energy band.

4. Data Analysis

Most past γ-ray analyses used H I data (single map or maps sorted by velocity), W_{CO} data, and dust data. The novelty of this work is to use H I line width information when preparing the $N_{\mathrm{H\,I}}$ maps. Specifically, we prepared $N_{\mathrm{H\,I}}$ maps of narrow H I and broad H I (Section 2) and assumed that the latter traces optically thin H I. As will be described in Section 4.1, we expect that narrow H I traces dark gas and confirm our expectation. We also find that there remains residual gas and employ a dust map to trace them (Section 4.2). Final modeling is described in Section 4.3.

[19] L is conventionally calculated as $\ln L = \sum_i n_i \ln(\theta_i) - \sum_i \theta_i$, where n_i and θ_i are the data and the model-predicted counts in each pixel (for each energy grid) denoted by the subscript, respectively (see, e.g., Mattox et al. 1996).

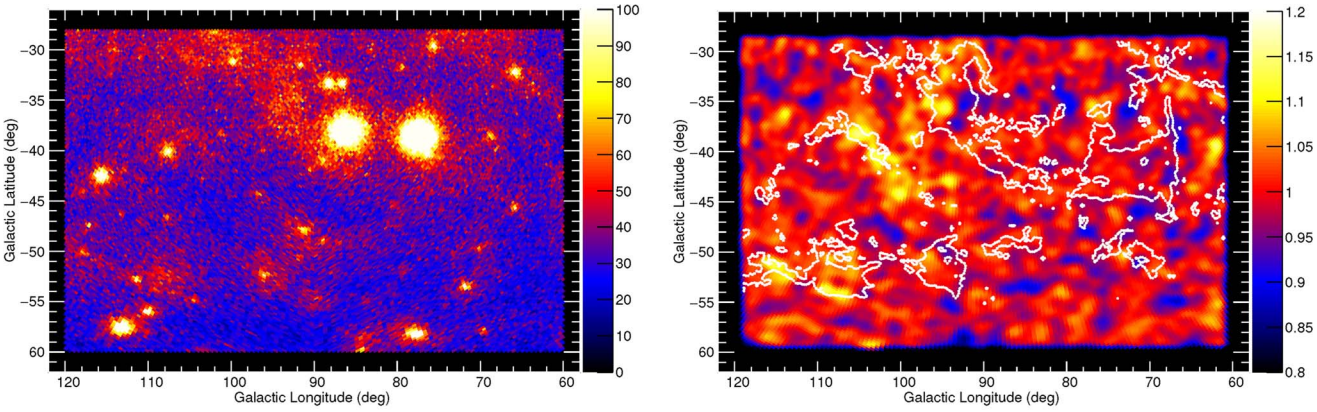

Figure 3. (a) Data count map. (b) Data/model ratio map using the baseline gas model. To accommodate small photon statistics (large statistical errors), panel (b) was smoothed using a Gaussian kernel with a standard deviation of $\sigma = 60'$. Contours of $R = 18 \times 10^{-8}$ W m^{-2} sr^{-1} are overlaid to indicate ISM structures.

4.1. Initial Modeling

To examine how well the narrow H I traces the dark gas, either optically thick H I (directly) or CO-dark H_2 (indirectly), we started our analysis of γ-ray data (Figure 3(a)) using the three H I maps and the W_{CO} map shown in Figure 1 (hereafter called the "baseline model") as gas templates. This is equivalent to setting $C_{dust} = 0$ in Equation (1), while the other coefficients ($C_{H\,I,i}$ and C_{CO}) are free to vary. Hereafter, we will use $C_{HI,1}$, $C_{H\,I,2}$, and $C_{H\,I,3}$ to represent the fitted coefficients for IVC, narrow H I, and broad H I, respectively. We adopted the optically thin approximation to convert W_{HI} into $N_{H\,I}$. If broad H I and narrow H I trace the optically thin H I and the dark gas (either optically thick H I or CO-dark H_2), respectively, well, we will have a larger emissivity for the latter and a flat fit-residual. Indeed, we observed that narrow H I gives about a 2 times larger emissivity ($C_{H\,I,2} \sim 2C_{H\,I,3}$). However, we found that our baseline model shows coherent residuals[20] in both the MBM 53–55 clouds and the Pegasus loop, as shown in Figure 3(b). There, we overlaid contours of $R = 18 \times 10^{-8}$ W m^{-2} sr^{-1} to indicate ISM structures. Considering that Fermi-LAT has a very large field of view and has continuously scanned the whole sky for more than a decade and is well calibrated accordingly (Section 3.1), such residuals cannot be attributed to the instrumental uncertainty of the γ-ray data. This indicates that our baseline model does not fully trace all the neutral gas, particularly in those ISM structures. We also applied the T_D-dependent correction proposed by Kalberla et al. (2020; Equation (7) in their paper) to the (narrow + broad H I) map to construct the summed column density map and used it to fit the γ-ray data. However, we obtained residuals very similar to that in Figure 3(b). Therefore, some fraction of gas is missed by H I 21 cm lines, even if we adopt the T_D-dependent correction of Kalberla et al. (2020). This motivated us to employ a dust map to model this residual gas. To determine which dust model to use, we tested single model maps of the total gas column density (N_H^{tot}) proportional to R or τ_{353} (from Planck Data Release 1 and 2). This is equivalent to setting $C_{H\,I,i} = 0$ and $C_{CO} = 0$. Although there are fewer degrees of freedom, each dust map gives a larger value of $\ln L$ than does our baseline gas model. Therefore, we concluded that we can use a dust map to estimate the residual gas not accounted for by the H I lines or W_{CO}. We interpret this residual gas being CO-dark H_2. Since both τ_{353} and R have potential issues as a tracer of the total gas column density (see, e.g., Mizuno et al. 2016, and references therein), we referred to $\ln L$ to determine which dust model to use. We found that the R map from Planck Data Release 1 gives the best fit among the four "single gas model maps", and hence we use it to construct the residual gas template. In the following section, we will construct a residual gas template and also examine if a model with the residual gas template gives a better fit than the model using a single dust map.

[20] Specifically, we refer to residuals at around $(l, b) \sim (96°, -35°)$, $(105°, -38°)$, $(103°, -40.5°)$, $(116°, -51°)$, and $(108°, -54°)$. They positionally coincide with the MBM 53–55 clouds and the Pegasus loop seen in the narrow H I map (Figure 1(b)) and dust R map (Figure 2(a)).

4.2. Fit with the Residual-gas Template

Having confirmed that our baseline gas model (the three W_{HI} maps, divided by using the H I line profiles, and the W_{CO} map) is not good enough to reproduce the γ-ray data, we added a residual gas template obtained by using the R map from Planck Data Release 1. To construct a good template, we examined the correlations among the H I, W_{CO}, and the dust maps in our ROI stored in a HEALPix map of order 9 (see Section 2). To match the resolution of the W_{HI} map, we smoothed the dust maps using a Gaussian kernel with an FWHM of $15\farcm4$. Since the W_{CO} data have worse resolution and cover a small fraction of the ROI, we allowed them to retain their original resolution. Then, by studying the gas properties in detail, we removed gas phases other than the residual gas from the H I and R data, and constructed the residual gas template as follows. To reduce contamination from CO-bright H_2, we required $W_{CO} \leqslant 0.1$ K km s^{-1}, except in the third step (subtraction of CO-bright H_2). Unlike the H I data, we could not distinguish different gas phases in a dust map along the line of sight using velocity information. Instead, we used T_d to separate the gas phases as described below. We aimed to identify optically thin H I, and since the γ-ray data have been generally reproduced by models using H I column densities assuming a high T_s ($\geqslant$125 K), W_{CO}, and a residual gas template (see, e.g., Remy et al. 2017, and references therein), we assumed linearity between W_{HI} and R at this stage.

Subtraction of the IVCs: we examined the W_{HI}(total) versus R (total) correlation and found that the outliers in the correlation at around $R\,(10^{-8}$ W m^{-2} sr$^{-1}) \sim 10$ and W_{HI}(K km s$^{-1}) \sim 350$ are affected by IVCs, as shown in

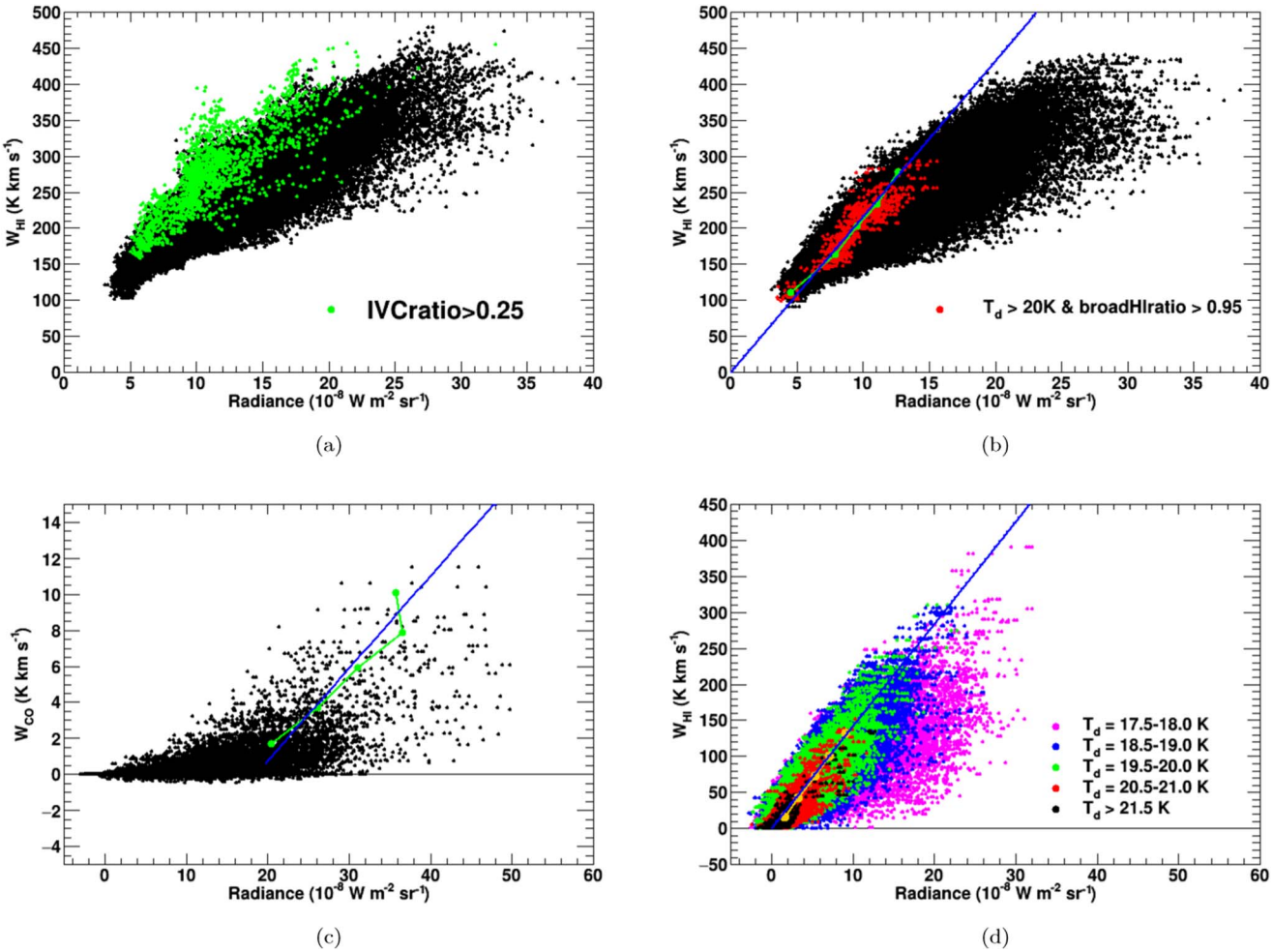

Figure 4. Correlation of the ISM gas in our ROI. Each point represents each pixel of our HEALPix map. (a) $W_{\rm HI}$(total)-R(total) correlation. Pixels with large IVC fractions are colored green. (b) $W_{\rm H\,I,2+3}$-R(total) correlation after subtracting the IVCs. Areas with large broad H I fractions and high $T_{\rm d}$ are colored red. The averages of $W_{\rm HI}$ and R in the $W_{\rm HI}$ bins are shown by green points. (c) $W_{\rm CO}$-$R_{\rm 2+CO+res}$ correlation after subtracting the broad H I. The averages of $W_{\rm CO}$ and R in $W_{\rm CO}$ bins are shown by green points. (d) $W_{\rm H\,I,2}$-$R_{\rm 2+res}$ correlation after subtracting the CO-bright H_2. The data are shown in 0.5 K ranges of $T_{\rm d}$ with 0.5 K gaps between intervals for clarity. The averages of $W_{\rm HI}$ and R in *the* $W_{\rm HI}$ bins are shown by orange points. In panels (b), (c), and (d), the best-fit linear relations are shown by blue lines. To reduce contamination from the CO-bright H_2, we required $W_{\rm CO} \leqslant 0.1$ K km s^{-1} except in panel (c). See the main text for details of the procedures used to construct the residual-gas template.

Figure 4(a). Most of the pixels with a high IVC fraction (i.e., the fractional $W_{\rm HI}$ of the IVC is more than 25%, represented by the green points) exhibit higher $W_{\rm HI}/R$ ratios than the average. We understand that this is because the IVCs in our ROI are dust poor (e.g., Fukui et al. 2021). While the true $W_{\rm HI}/R$ ratio of the IVCs is uncertain, their contribution to the gas density is small (the integral of $W_{\rm HI}$ is at the 5% level; see Mizuno et al. 2016). Therefore, for simplicity, we removed the IVCs from the $W_{\rm HI}$ and R maps, assuming that they do not have dust (i.e., we subtracted the column density of the IVCs from $W_{\rm HI}$, while keeping the value of R for each pixel). Unchanging R would overestimate the other gas components, but the effect is minor since the IVCs' contribution is small and their spatial distribution (Figure 1(a)) is very different from that of the other gas phases. Now we have a $W_{\rm HI}$ map of narrow and broad H I (hereafter called $W_{\rm H\,I,2+3}$).

Subtraction of the broad H I: then we examined the $W_{\rm H\,I,2+3}$ versus R(total) correlation (Figure 4(b)). We first aimed to evaluate $R/W_{\rm HI}$ ratio of broad H I, and selected areas rich in broad H I (i.e., with the fractional $W_{\rm HI}$ of broad H I more than 95%). Narrow H I will have a larger $N_{\rm H}/W_{\rm HI}$ ratio (where $N_{\rm H}$ is the column density of each gas phase) than broad H I does if it is optically thick. CO-dark H_2 will have an even larger $N_{\rm H}/W_{\rm HI}$ ratio. They will have a larger $R/W_{\rm HI}$ ratio, and may not be removed well by the $W_{\rm HI}$-based selection. Such excess gas (over optically thin H I) has been found toward the directions of low $T_{\rm d}$ (e.g., Mizuno et al. 2016; Hayashi et al. 2019). As described by Fukui et al. (2014), both the H I gas and dust are heated by the ISRF and hence are expected to have a positive correlation between their temperatures. Therefore optically thick H I will be found primarily in the low-$T_{\rm d}$ area. CO-dark H_2 could also have a similar dependence on $T_{\rm d}$. Therefore, to reduce further the possible contamination from optically thick H I and CO-dark H_2, we also required these areas to have $T_{\rm d} \geqslant 20$ K (the red points in the panel). We then calculated the average of $W_{\rm HI}$ and R in every 40 K km s^{-1} bin from $W_{\rm HI} = 100$ to 300 K km s^{-1} and obtained the linear relation $R\,(10^{-8}\,{\rm W\,m^{-2}\,sr^{-1}}) = 0.0463 \cdot {\rm W_{HI}(K\,km\,s^{-1})}$. We interpreted that this gives the $R/W_{\rm HI}$ ratio of broad H I gas and subtracted it from the $W_{\rm H\,I,2+3}$ and R(total) maps using this ratio. We note that changing the threshold of $T_{\rm d}$ by $\pm$ 1 K affects the ratio by

less than 5%, confirming that a specific choice of the T_d threshold does not affect the final map significantly. Now we have a W_{HI} map of narrow H I ($W_{H\,I,2}$), and an R map associated with narrow H I, CO-bright H_2 and residual gas ($R_{2+CO+res}$).

Subtraction of the CO-bright H_2: we then examined the W_{CO} and $R_{2+CO+res}$ correlation. To select W_{CO}-rich areas, we required W_{CO} to be greater than 1 K km s^{-1}. We then calculated the averages of W_{CO} and R in every 2 K km s^{-1} bin from $W_{CO} = 1$ to 12 K km s^{-1} (the last bin spans from 9 to 12 K km s^{-1}) and fitted them with a linear relation with an offset. Since dark gas lies around CO clouds (e.g., Grenier et al. 2005), their contribution was mainly attributed to the offset. We obtained the linear relation $R\,(10^{-8}\,\mathrm{W\,m^{-2}\,sr^{-1}}) = 18.5 + 1.95 \cdot \mathrm{W_{CO}(K\,km\,s^{-1})}$, and subtracted the CO-bright H_2 gas from the $R_{2+CO+res}$ map using the obtained coefficient. Although there is a significant scatter in Figure 4(c) and hence the uncertainty of R/W_{CO} ratio is large, the effect on the ISM gas properties is small (except for the CO-bright H_2) as will be described in Section 5.1. Now we have an R map associated with narrow H I and the residual gas (R_{2+res}).

Subtraction of the narrow H I: the correlation between $W_{H\,I,2}$ and R_{2+res}, sorted by T_d is shown in Figure 4(d). In order to remove the narrow H I gas, we first aimed to evaluate its R/W_{HI} ratio. In Figure 4(d), we found that areas with low T_d exhibit a high R/W_{HI} ratio, which we interpreted as being the residual gas we found in Section 4.1. To reduce their contamination, we selected high-T_d areas (T_d more than 20 K). We then calculated the average of W_{HI} and R in every 30 K km s^{-1} bin from $W_{HI} = 0$ to 150 K km s^{-1}, and we obtained the linear relation $R\,(10^{-8}\,\mathrm{W\,m^{-2}\,sr^{-1}}) = 0.0705 \cdot \mathrm{W_{HI}(K\,km\,s^{-1})}$. We removed narrow H I from the R_{2+res} map using this ratio. Now we have the residual gas template and we use it in the γ-ray data analysis. If T_s is high throughout H I, as claimed by several past studies, this analysis will give similar emissivities for broad and narrow H I templates.

The residual gas template improves the fit significantly; the residuals seen in the MBM 53–55 clouds and the Pegasus loop are reduced significantly, and the value of $\ln L$ increased by 337.5 with 10° of freedom. Therefore the residual gas template successfully reproduces the gas not traced by our baseline model. The model with the residual gas template gives $\Delta \ln L = 103.4$ with 20 more degrees of freedom than the model using single R (of Planck Data Release 1). We also found that narrow H I gives about 1.5 times larger emissivity than that of broad H I ($C_{H\,I,2} \sim 1.5 C_{H\,I,3}$). We understand that this is because the narrow H I is optically thick, and we apply a correction for this in calculating the gas column density.

4.3. Final Modeling with the T_s Corrections

We applied a spin–temperature correction to the gas column density based on Fukui et al. (2014) and Hayashi et al. (2019) to construct new narrow H I templates and residual gas templates. For simplicity, we assumed that the peak brightness temperature (T_p) is representative of the brightness temperature along the line of sight. Then, the radiation transfer equation gives W_{HI} and the optical depth $\tau_{H\,I}$ of the H I gas as a function of T_s and $\Delta V_{H\,I} (\equiv W_{HI}/T_p)$ as

$$W_{HI}(\mathrm{K\,km\,s^{-1}}) = [T_s(\mathrm{K}) - T_{bg}(\mathrm{K})] \cdot \Delta V_{H\,I}(\mathrm{km\,s^{-1}}) \cdot [1 - \exp(-\tau_{H\,I})], \quad (2)$$

and

$$\tau_{H\,I} = \frac{N_{H\,I}(\mathrm{cm^{-2}})}{1.82 \times 10^{18}} \cdot \frac{1}{T_s(\mathrm{K})} \cdot \frac{1}{\Delta V_{H\,I}(\mathrm{km\,s^{-1}})}, \quad (3)$$

where T_{bg} is the background continuum radiation temperature and $N_{H\,I}$ is the gas column density of H I gas. Then, we can calculate $N_{H\,I}$ as

$$N_{H\,I} = -1.82 \times 10^{18} \cdot T_s(\mathrm{K}) \cdot \Delta V_{H\,I}(\mathrm{km\,s^{-1}}) \cdot \log\left[1 - \frac{W_{HI}(\mathrm{K\,km\,s^{-1}})}{[T_s(\mathrm{K}) - T_{bg}(\mathrm{K})] \cdot \Delta V_{H\,I}(\mathrm{km\,s^{-1}})}\right]. \quad (4)$$

We calculated the value of $N_{H\,I}$ for the narrow H I using Equation (4), assuming a uniform T_s over the ROI and $T_{bg} = 2.7$ K (the temperature of the cosmic microwave background radiation). We note that using a single brightness temperature along the line of sight and a uniform T_s over the ROI is a rough approximation that may introduce over- or under-predictions at the pixel level. Also, we compared the data and the model of Gaussian decomposition for several pixels with a complex profile (the number of Gaussians was more than seven; see Kalberla & Haud 2018) and found that parameters of the narrow lines could be affected by dominant broad lines there. Therefore, the value of T_s should not be taken at face value. It is a reasonable approach, though, considering the low photon statistics of the γ-ray data. Also, it allows us for the first time to apply different T_s corrections to the different H I gas phases used in the γ-ray data analysis.

We constructed $N_{H\,I}$ maps of narrow H I assuming $T_s = 120$ to 30 K in 10 K steps. If $T_p > T_s - T_{bg}$, Equation (4) diverges to infinity. In such a case, we stopped at a T_s value that gives $\tau_{H\,I} = 3$ in Equation (2), and calculated $N_{H\,I}$ using Equation (4). $T_p > T_s - T_{bg}$ was found only in a small fraction of pixels (less than 0.1%) for $T_s \leqslant 40$ K. We then constructed a residual gas template for each T_s. Specifically, we replaced W_{HI} in Figure 4(d) with $N_{H\,I}(\mathrm{cm^{-2}})/(1.82 \times 10^{18})$. Although the difference in $\ln L$ is small, we confirmed that the fit improves gradually as we apply corrections with lower values of T_s down to $T_s = 40$ K. We therefore concluded that the templates with a T_s correction of 40 K applied to narrow H I represent our best model, and we adopted them as our final model. The emissivity of narrow H I now agrees with that of broad H I at the 10% level. Specifically, the averages of $C_{H\,I,2}$ (narrow H I) and $C_{H\,I,3}$ (broad H I) are 0.980 ± 0.018 and 0.866 ± 0.030, respectively, giving the ratio of narrow H I:broad H I = 1.13. The model count map and the data/model ratio map are shown in Figure 5. In comparison with Figure 3, we can confirm that the residuals are reduced significantly. A summary of the emissivity spectrum and the spectrum of each component is presented in Figure 6, and the best-fit parameters are summarized in Table 1. Although the spectral shapes of the CO-bright H_2 and IVC are apparently different from those of other gas templates, they are minor components and the errors are large, and hence the effect on the other components is small. Also, although the IC spectrum shows unphysical fluctuations, it anticorrelates with the isotropic spectrum. Therefore, most of uncertainties of the

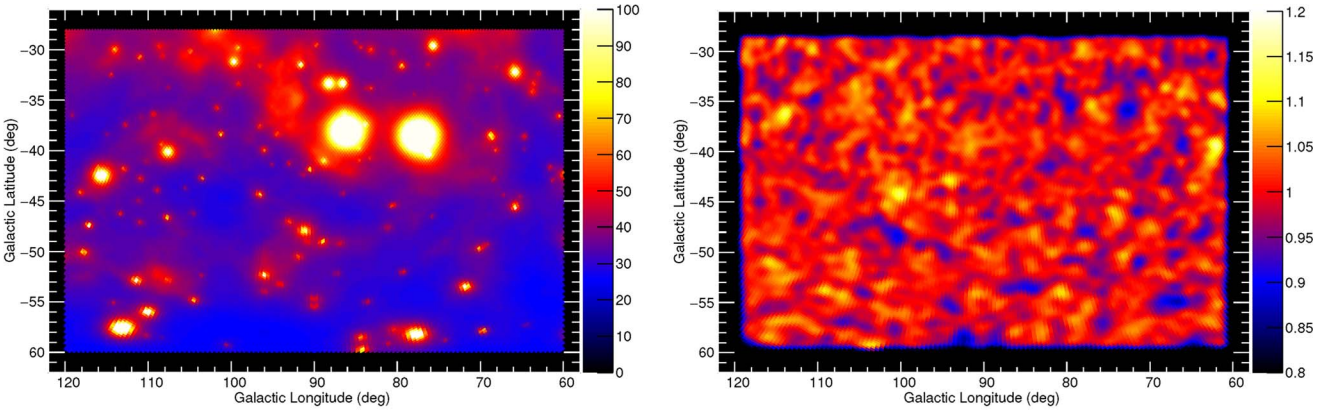

(a) (b)

Figure 5. (a) Model count map. (b) Data/model ratio map. Both maps are obtained with a T_s correction (of 40 K) applied to the narrow H I template. Panel (b) is smoothed using a Gaussian kernel with $\sigma = 60'$ for display.

Table 1
Best-fit Parameters, with 1σ Statistical Uncertainties, Obtained by using Gas Templates with a T_s Correction of 40 K to the Narrow H I

Energy (GeV)	$C_{\rm HI,1}$ (IVC)	$C_{\rm H\,I,2}$ (narrow H I)	$C_{\rm H\,I,3}$ (broad H I)	$C_{\rm CO}$	$C_{\rm dust}$	$C_{\rm IC}$	$C_{\rm iso}$
0.10–0.17	0.97 ± 0.30	0.70 ± 0.08	0.93 ± 0.09	0.58 ± 0.25	0.18 ± 0.04	0.70 ± 0.11	1.18 ± 0.05
0.17–0.30	0.68 ± 0.21	0.84 ± 0.05	0.81 ± 0.08	0.37 ± 0.15	0.19 ± 0.03	0.89 ± 0.13	1.20 ± 0.06
0.30–0.52	0.66 ± 0.15	0.86 ± 0.04	0.88 ± 0.06	0.34 ± 0.10	0.22 ± 0.02	0.99 ± 0.12	1.25 ± 0.06
0.52–0.90	0.60 ± 0.15	1.10 ± 0.04	0.93 ± 0.07	0.42 ± 0.09	0.22 ± 0.02	1.26 ± 0.15	1.04 ± 0.07
0.90–1.56	0.41 ± 0.17	1.12 ± 0.04	0.74 ± 0.08	0.51 ± 0.09	0.22 ± 0.02	1.67 ± 0.18	1.06 ± 0.09
1.56–2.70	0.86 ± 0.21	0.98 ± 0.06	0.95 ± 0.10	0.40 ± 0.11	0.24 ± 0.02	0.79 ± 0.24	1.44 ± 0.13
2.70–4.68	0.22 ± 0.32	1.07 ± 0.08	0.95 ± 0.14	0.93 ± 0.18	0.20 ± 0.03	1.34 ± 0.34	1.19 ± 0.16
4.68–8.10	1.29 ± 0.54	1.13 ± 0.14	0.61 ± 0.23	0.82 ± 0.27	0.18 ± 0.05	2.26 ± 0.49	0.92 ± 0.20
8.10–24.3	0.13 ± 0.77	0.97 ± 0.19	0.69 ± 0.31	0.46 ± 0.35	0.24 ± 0.07	1.66 ± 0.58	1.06 ± 0.20
24.3–72.9	1.80 ± 2.21	1.06 ± 0.54	1.44 ± 0.84	0.00 ± 0.03	0.45 ± 0.17	2.68 ± 1.12	0.27 ± 0.43

IC and the isotropic emission (both have smooth spatial distributions) are mutually absorbed and have a small impact on the gas emissivities.

5. Discussion

5.1. ISM Properties

Assuming a uniform CR intensity, we can evaluate the column density of each gas phase. We tabulated $N_{\rm H}$ integrated over the ROI in Table 2, where $\int N_{\rm H}\, d\Omega$ for broad H I was calculated assuming the optically thin case. The corresponding value of narrow H I was calculated with $T_s = 40$ K. As described in Section 4.2, the emissivity ratio of narrow H I to broad H I is 1.13. We interpret this to mean that while the template map of broad H I represents optically thin H I distribution, that of narrow H I with $T_s = 40$ K still underpredicts the true gas column density. Therefore we took this ratio into account in the calculation (i.e., the true $N_{\rm H}$ of narrow H I is 13% larger.) We also calculated the integral of $N_{\rm H}$ for other gas phases using the average fitting coefficients given in Table 1. Although the $R/W_{\rm CO}$ ratio has a large uncertainy (see Section 4.2), its effect on other gas phases is expected to be small since CO-bright H_2 is the least significant component in our ROI (Table 2). To examine this expectation, we increased/decreased the $R/W_{\rm CO}$ ratio by a factor of 2 and repeated the analysis (construction of the residual gas template and γ-ray fit with it). While $C_{\rm CO}$ changed by $\sim 20\%$, the fit coefficients of other gas components were affected only at the 1% level.

Table 2
Integral for $N_{\rm H}$ of Each Gas Phase

Phase	$\int N_{\rm H}\, d\Omega$ (10^{22} cm^{-2} deg^2)
broad H I	39.9
narrow H I	26.1 (8.0 over the thin-H I case)
IVC	2.8
residual gas	7.9
CO-bright H_2	1.1

Because the MBM 53–55 clouds and the Pegasus loop are located at similar distances from the solar system, and because most H I clouds are expected to coexist with H_2 clouds (because they are located at high Galactic latitudes), we can estimate the total mass of gas from $N_{\rm H}$ as

$$M = \mu m_{\rm H} d^2 \int N_{\rm H}\, d\Omega, \tag{5}$$

where d is the distance to the cloud, $m_{\rm H}$ is the mass of the hydrogen atom, and $\mu = 1.41$ is the mean atomic mass per H atom (Däppen 2000). From Equation (5), $\int N_{\rm H}\, d\Omega = 10^{22}$ cm^{-2} deg^2 corresponds to $\sim 740\, M_\odot$ for $d = 150$ pc (Welty et al. 1989). Therefore the mass of broad H I is estimated to be $\sim 3 \times 10^4\, M_\odot$.

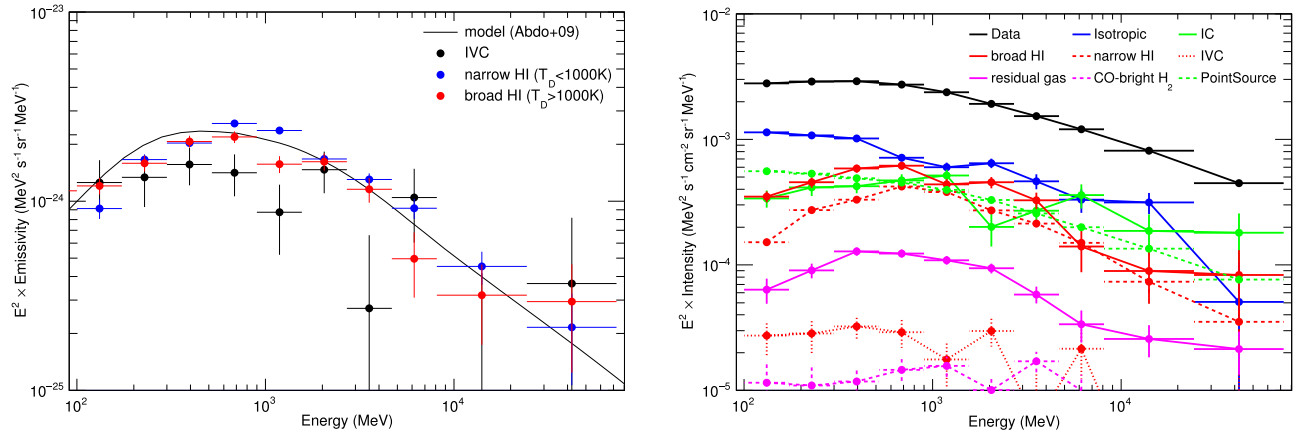

(a) (b)

Figure 6. (a) H I emissivity spectra of the IVC, narrow H I, and broad H I. (b) Spectrum of each component. Both panels are obtained by applying T_s corrections of 40 K to the narrow H I.

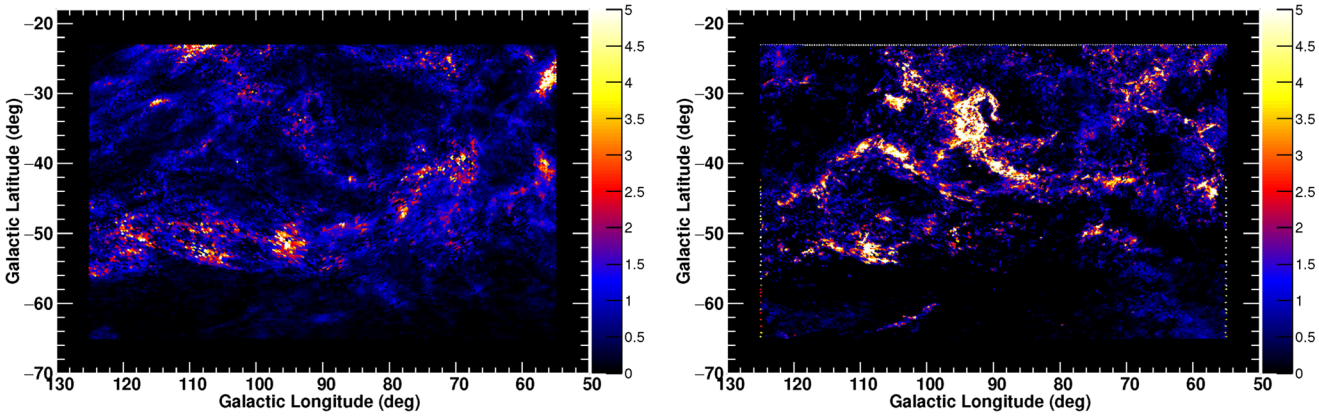

(a) (b)

Figure 7. (a) Column density distribution of the H I optical depth correction and (b) that of the CO-dark H_2. Both distributions are obtained by using the analysis with a T_s correction of 40 K to the narrow-H I template, and shown in 10^{20} cm^{-2}.

We interpret the broad H I to be optically thin, narrow H I to be optically thick, and the residual gas to be CO-dark H_2. The values of $\int N_H\, d\Omega$ for the narrow H I are larger than that of the optically thin case by 8.0×10^{22} cm^{-2} deg^2, nearly equal to that of the residual gas. Therefore, the ratio of optical depth correction (to the H I column density) to CO-dark H_2 is $\sim$1. Because of the lack of information on T_s, this value has been used by several authors as a possible case when discussing ISM properties (e.g., Planck Collaboration XXVIII 2015; Remy et al. 2018), and our result supports their assumption. The fraction of the H I optical depth correction and CO-dark H_2, usually considered dark gas, is about 20% of the total gas column density. This agrees with the value obtained by Mizuno et al. (2016), who employed a different gas-modeling method.

We summarize the spatial distribution of dark gas in Figure 7. The left panel shows the distribution of the H I optical depth correction, and the right panel shows that of the CO-dark H_2 in N_H. They show the different gas distributions and may help us understand how the gas evolves from thin H I to CO-bright H_2 through two dark-gas phases (optically thick H I and CO-dark H_2). The CO-dark H_2 clearly traces the MBM 53–55 clouds and the Pegasus loop well, with similar N_H peaks in the two regions. On the other hand, the H I optical depth correction (left panel) shows a similar but less structured distribution, with a larger amount of the gas in the Pegasus loop.

Table 3
Integral for N_H (10^{22} cm^{-2} deg^2) for the Two Subregions

Region	H I Optical Depth Correction	CO-dark H_2	CO-bright H_2
MBM 53–55	0.7	2.3	0.8
Pegasus loop	1.8	1.9	0.1

To examine the gas distributions in more detail, we defined two subregions, the MBM 53–55 clouds and the Pegasus loop, as $l = 84°$ to 96° and $b = -44°$ to $-30°$ and $l = 99°$ to 109° and $b = -55°$ to $-35°$, respectively. Then we calculated the integral of the column density of each gas phase as summarized in Table 3. These results give a CO-dark H_2 fraction, defined as the ratio of CO-dark H_2 to total H_2, of 0.75 and more than 0.9 for the MBM 53–55 clouds and the Pegasus loop, respectively. These values are larger than typical values (0.3–0.5) obtained by the Planck collaboration through dust-emission observations of high-latitude areas and that found by Wolfire et al. (2010) through simulations. In other words, the MBM 53–55 clouds

Table 4
Emissivity Multiplied by E^2

Energy (GeV)	$E^2 \times$ Emissivity (10^{-24} MeV^2 s^{-1} sr^{-1} MeV^{-1})
0.10–0.17	1.00 ± 0.06
0.17–0.30	1.51 ± 0.07
0.30–0.52	1.86 ± 0.06
0.52–0.90	2.26 ± 0.07
0.90–1.56	1.98 ± 0.07
1.56–2.70	1.51 ± 0.07
2.70–4.68	1.15 ± 0.08
4.68–8.10	0.74 ± 0.09
8.10–24.3	0.38 ± 0.07
24.3–72.9	0.21 ± 0.09

and Pegasus loop were found to be rich in dark gas when normalized by total H_2.

A possible explanation of such a large CO-dark H_2 fraction is due to the small gas column density that results in CO photodissociation. The value of N_H we found is a few $\times$ 10^{21} cm^{-2} (Figure 7). On the other hand, Wolfire et al. (2010) assumed clouds with a larger column density ($\geqslant 10^{22}$ cm^{-2}) and modeled the gas distribution using a photodissociation region code. We also note that Smith et al. (2004) predict that the CO-dark H_2 fraction anticorrelates with the molecular gas column density, and W_{CO} drops (the CO-dark H_2 fraction increases) below a column density of a few $\times$ 10^{21} cm^{-2}. Indeed, Remy et al. (2018) reported that the CO-dark H_2 fraction increases below the column density around this value in anticenter clouds.

In summary, the amounts of gas in the H I optical depth correction and CO-dark H_2 are similar in the Pegasus loop. The column density of H_2 is above the threshold (a few $\times$ 10^{21} cm^{-2}) only in thin and filamentary structures, and hence, the molecular gas is predominantly CO-dark. On the other hand, the dark gas in the MBM 53–55 clouds is mostly the CO-dark H_2 phase. The column density is above the threshold in large areas, and hence, the CO-bright H_2 starts to form, and the CO-dark H_2 fraction starts to decrease.

We remind the reader that the discussion above depends on the assumption that the broad H I and narrow H I correspond to the optically thin H I and thick H I, respectively. This assumption is based on our findings that (1) narrow H I gives a $\sim$1.5 times larger emissivity than that of broad H I, and (2) there remains residual gas not accounted for by the H I 21 cm lines. The discussion above also depends on our (simplified) optical depth correction to narrow H I using Equation (4). Systematic and large surveys of background radio sources will provide measurements of the H I optical depth and the ultimate answer to the gas phases. Such large surveys, however, may not be feasible to cover all nearby cloud complexes. Therefore, an analysis using γ-rays, such as the one presented here, is complementary and worthwhile.

5.2. CR Properties

Finally, we discuss the H I emissivity spectrum and the inferred CR spectrum obtained in this study. Their properties can be evaluated in more detail with fewer gas templates. Therefore, we added the narrow H I (with the T_s correction) and broad H I templates and reworked the γ-ray fitting. The obtained emissivity spectrum is summarized in Table 4 and Figure 8(a), together with those of other relevant studies (Casandjian 2015; Mizuno et al. 2020) and the emissivity model for the proton local interstellar spectrum (LIS) used in this study. Since we required the fit coefficient ratio of the narrow H I to broad H I to be 1.0, we take the error of the latter ($\sim$4%) as the systematic uncertainty of the emissivity. We also consider the LAT effective area uncertainty;[21] we assume the uncertainty to be 3% above 300 MeV, and 6% below 300 MeV where we used only PSF event types 2 and 3. By adding these two types of systematics in quadrature, we obtained the overall uncertainty to be 5% and 7% above and below 300 MeV, respectively. Even if these systematic uncertainties are taken into account, our emissivity is lower than those of other studies. Also, while it agrees with the model above 1 GeV, we can recognize a small deviation at low energies. This suggests that there is a spectral break at around a few GeV that is stronger than that in the model. We note that Mizuno et al. (2016) found a hint of a similar deviation, although they could not give a firm conclusion since their analysis was limited to above 300 MeV.

To investigate the inferred CR spectrum in more detail, we carried out simultaneous fitting of the proton and He CR observations and the γ-ray emissivity. We modeled the LIS and the solar-modulation effect using analytical formulae and then used a Markov chain Monte Carlo (MCMC) technique to constrain the model parameters; see Appendix C for details of the framework. The proton and He LIS models, $J(p)$, are expressed as a power law in momentum (p) with two breaks

$$J(p) \propto \left[\left(\frac{p}{p_{\rm br1}}\right)^{\alpha_1/\delta_1} + \left(\frac{p}{p_{\rm br1}}\right)^{\alpha_2/\delta_1}\right]^{-\delta_1} \cdot \left[1 + \left(\frac{p}{p_{\rm br2}}\right)^{\alpha_3/\delta_2}\right]^{-\delta_2}. \quad (6)$$

Here, α_1 and α_2 are the indices in the high- and medium-energy ranges, respectively, and $p_{\rm br1}$ and δ_1 control the first (high energy) spectral break, which is presumably due to a break in the interstellar diffusion coefficient (e.g., Ptuskin et al. 2006). The parameters $p_{\rm br2}$ and δ_2 control the second break, which represents an expected break due to ionization (e.g., Cummings et al. 2016), and α_3 is the difference in the index over this break. Our formula is motivated by the work by Strong (2015), but it includes more parameters to represent the CR (and γ-ray) data over a broader energy range. It is still simple and hence allows us to fit to the data within a reasonable computation time.

The γ-ray emissivity is calculated, based on the proton and He LIS models, using the AAfrag package (Kachelriess et al. 2019) and parameterizations in Kamae et al. (2006). We also add an electron/positron bremsstrahlung model of Orlando (2018), specifically their best propagation model called PDDE. In that work, constraints on the electron/positron LIS were obtained by fitting the CR direct measurements, the local synchrotron emission from radio to microwaves, and the local γ-ray emissivity.

In the CR and γ-ray modeling, we used nine proton data sets, including the AMS-02 data (from 2011 to 2013) and the Voyager 1 data (from 2012). We also used five He data sets, including the AMS-02 and Voyager 1 data from the same

[21] https://fermi.gsfc.nasa.gov/ssc/data/analysis/LAT_caveats.html

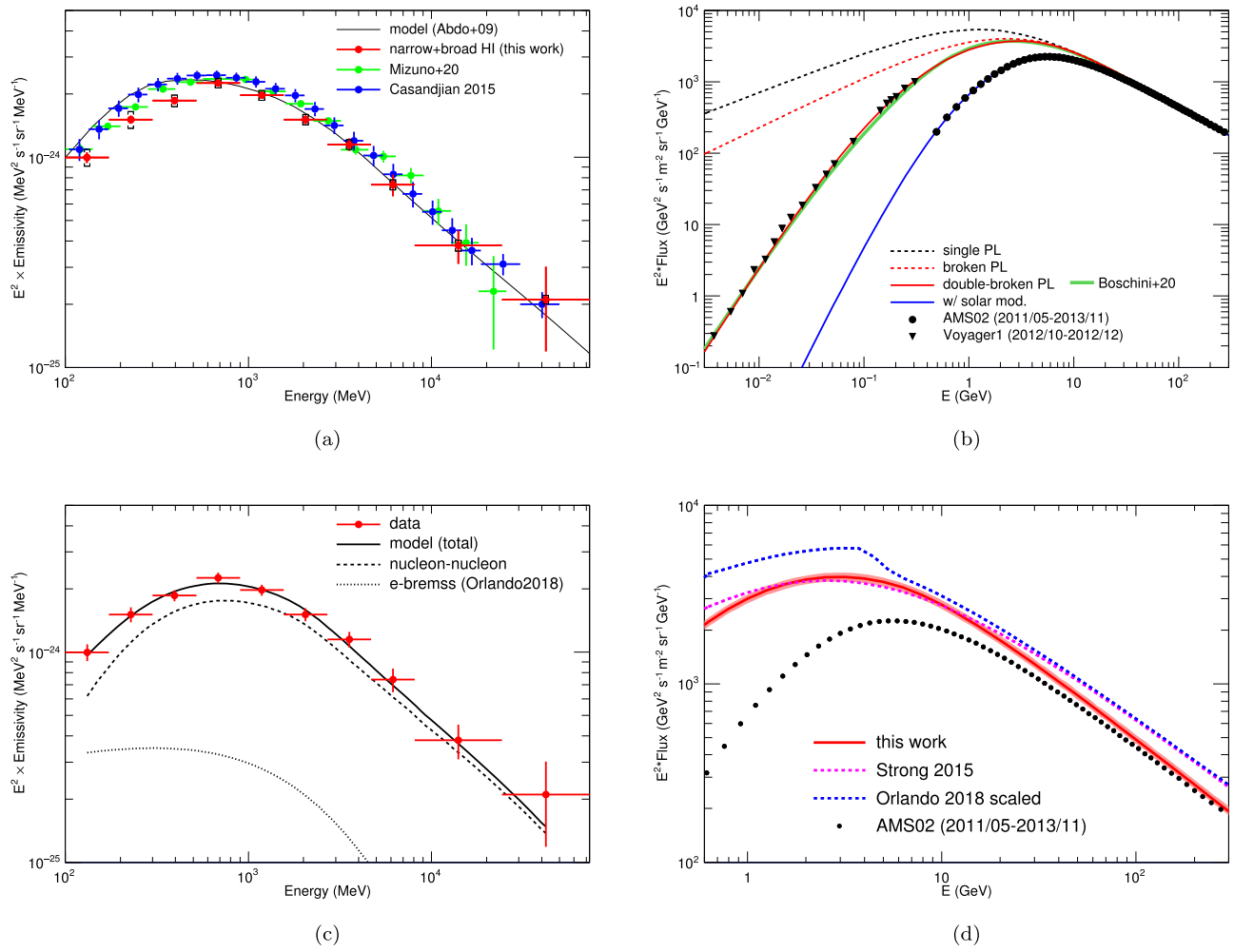

Figure 8. (a) H I emissivity spectrum obtained in this study (red points) compared with the model curve and the results of relevant studies from Fermi-LAT (Casandjian 2015; Mizuno et al. 2020). Square brackets represent the systematic errors. The emissivity model adopted in this analysis is also shown as a solid black line. (b) CR proton LIS obtained by fitting the CR and γ-ray data. The LIS and the spectrum at the Earth are shown by the solid red and blue lines, respectively. For reference, a spectrum without a break and one with only a high-energy break are shown by the dotted black and red lines, respectively. The spectrum obtained by Boschini et al. (2020) is shown by the green line for comparison. (c) Emissivity model spectrum obtained by fitting the CR and γ-ray data. The data are shown with the statistical and systematic errors summed in quadrature. Contributions of hadronic interation and electron bremsstrahlung are indicated. See Appendix C for details of the model calculations. (d) Comparison of LIS models based on γ-ray emissivities (this work, that of Strong 2015, and that of Orlando 2018) in the GeV energy range. The AMS-02 data are also shown. Our LIS is multiplied by 1.07 to include the scaling factor for γ-rays. The LIS model of Strong (2015) has been obtained by fitting an analytical formula to the emissivity by Casandjian (2015), and that of Orlando (2018) has been obtained by scaling a CR propagation model called PDDE to fit the same emissivity spectrum. The uncertainty of our LIS is shown by a light-red shaded band. Those for Strong (2015) and Orlando (2018) are not presented for clarity.

periods. All the CR data were retrieved from the Cosmic-Ray Data Base (Maurin et al. 2014). We used CR data other than AMS-02 and Voyager 1 to disentangle a possible degeneracy between the LIS shape and solar modulation. See Appendix C for details. We then obtained the parameters of the LIS model as summarized in Table 5. Other miscellaneous parameters are given in Appendix C (Table 8). The inferred CR spectrum and γ-ray emissivity spectrum are shown in Figure 8(b) and Figure 8(c), respectively. The scaling factor for the γ-rays is 1.07 ± 0.03 relative to the AMS-02 spectrum. Our LIS parameters are primarily constrained by CR data that have very small errors. The proton spectrum from 1–100 GeV mainly contributes to the γ-ray emissivity in the Fermi-LAT energy band, and our model emissivity spectrum reproduces the data well, as shown in Figure 8(c). Our proton spectrum also agrees well with that of Boschini et al. (2020), which is

Table 5
Parameters of the LIS Obtained by Fitting the CR and γ-Ray Data

Parameter	Proton		He
Normalization	26.20 ± 0.10		1.41 ± 0.01
α_1	2.86 ± 0.01		2.76 ± 0.01
α_2		2.57 ± 0.02	
α_3	-3.25 ± 0.05		-2.73 ± 0.08
R_{br1} (GV)		7.08 ± 0.31	
δ_1		0.07 ± 0.01	
R_{br2} (GV)	0.524 ± 0.015		1.314 ± 0.061
δ_2	1.91 ± 0.07		0.82 ± 0.07

Note. Normalization is the flux [c s^{-1} m^{-2} sr^{-1} (GeV/n)$^{-1}$] at $p = 10$ GeV. CR protons and He are assumed to share the value of the high-energy spectral break in rigidity. Therefore breaks in rigidity ($R_{\rm br}$) are given instead of breaks in momentum.

based on CR data with a detailed calculation of the CR propagation in the heliosphere. This supports that our formula (Equation (6)) and force-field approximation well represent the LIS and the CR propagation in the heliosphere. The solar-modulation potential Φ was found to be about 615 MV for AMS-02. For the high-energy spectral break, we obtained $p_{\rm br1} = 7.1 \pm 0.3$ GeV and $\delta_1 = 0.07 \pm 0.01$, confirming earlier claims of this spectral break from γ-ray data (e.g., Strong 2015) and CR data (e.g., Ptuskin et al. 2006). We note that our break energy is somewhat larger than that inferred from the CR data using the secondary to primary ratio (usually 3–5 GeV). This may be due to a spectral break in the CR injection spectrum in addition to a break in the interstellar diffusion coefficient (e.g., Strong et al. 2007). A detailed comparison of our LIS model to the primary and secondary CR data may clarify this issue and help us better understand CR acceleration and propagation.

Recently, Strong (2015) and Orlando (2018) used the high-latitude γ-ray emissivity spectrum determined by Casandjian (2015) and obtained about a 30% larger proton LIS than that measured at the Earth in the high-energy region. The discrepancy is larger than the uncertainties (at the 10% level) of their studies. If it is true, the CR spectrum at the Earth is not representative of the LIS. To examine this issue we compared proton LIS models in the GeV energy range based on γ-ray data (and CR data) in Figure 8(d). Therein, our LIS model is multiplied by 1.07 to take account of the scaling factor for γ-rays, and shown with the statistical error (3%) and systematic error (5%) summed in quadrature As already shown in Figure 8(a), our emissivity is 10%–15% lower than that of Casandjian (2015), making the LIS model consistent with the AMS-02 spectrum within 10% at high energies where the solar modulation is irrelevant. Therefore, while the previous studies required an LIS larger than the PAMELA/AMS-02 spectra by ∼30%, our new study shows better agreement. We note that while Casandjian (2015) carried out detailed modeling of the high-latitude region and provided a very precise measurement of the γ-ray emissivity spectrum, they used Pass 7 data and assumed a uniform $T_{\rm s}$, and hence the obtained spectrum might suffer from bias on the absolute value. Also, it samples a region of around ∼1 kpc and hence may deviate from the prediction based on the CR spectrum directly measured at the Earth, while the MBM 53–55 clouds and the Pegasus loop are very close to us. Of course, our result is based on a particular region in the sky, and a systematic study of local regions is crucial to settle the issue. Such a systematic study is also crucial to investigate a possible local variation of the CR spectrum.

6. Summary

We carried out a detailed study of the ISM and CRs using Fermi-LAT data in the 0.3–72.9 GeV energy range at Galactic longitudes from 60° to 120° and Galactic latitudes from −60° to −28°. This region encompasses the MBM 53–55 clouds and the Pegusas loop. We improved the ISM gas modeling over our previous work by using Gaussian decomposition of the 21 cm line emission. We succeeded in distinguishing the optically thin H I, optically thick H I, and CO-dark H_2 gas phases. We found the fractions of H I optical depth correction and of CO-dark H_2 to be nearly equal, and we found the fraction of dark gas to be about 20% of the total gas column density. The CO-dark H_2 fraction is higher in the Pegasus loop than in the MBM 53–55 clouds, likely due to CO photodissociation. While the H I emissivity spectrum agrees with the adopted model of the LIS above 1 GeV, there is a small deviation below a few hundreds of MeV. We fitted the CR spectra measured at/near the Earth and the measured γ-ray spectrum simultaneously, and we obtained a spectral break in the proton LIS at ∼7 GeV. Our new emissivity spectrum relaxes the tension with the CR spectra directly measured at the Earth, and agrees with the AMS-02 spectrum within 10%.

The Fermi LAT Collaboration acknowledges generous ongoing support from a number of agencies and institutes that have supported both the development and the operation of the LAT as well as scientific data analysis. These include the National Aeronautics and Space Administration and the Department of Energy in the United States, the Commissariat à l'Energie Atomique and the Centre National de la Recherche Scientifique/Institut National de Physique Nucléaire et de Physique des Particules in France, the Agenzia Spaziale Italiana and the Istituto Nazionale di Fisica Nucleare in Italy, the Ministry of Education, Culture, Sports, Science and Technology (MEXT) and High Energy Accelerator Research Organization (KEK) in Japan, and the K. A. Wallenberg Foundation, the Swedish Research Council, and the Swedish National Space Board in Sweden.

Additional support for the science analysis during the operations phase is gratefully acknowledged from the Istituto Nazionale di Astrofisica in Italy and the Centre National d'Études Spatiales in France. This work performed in part under DOE Contract DE-AC02-76SF00515.

This work was partially supported by JSPS Grants-in-Aid for Scientific Research (KAKENHI) grant No. 17H02866 (T.M.) and by Core of Research for the Energetic Universe at Hiroshima University. E.O. acknowledges the ASI-INAF agreement No. 2017-14-H.0 and the NASA grant No. 80NSSC22K0495 GALPROP development is partially supported through NASA grant NNX17AB48G.

Software: emcee (Foreman-Mackey et al. 2013), Fermitools (v2.0.0; Fermi Science Support Development Team 2019), AAfrag (Kachelriess et al. 2019).

Appendix A
Treatment of the Infrared Sources

In the Planck dust-model maps from Data Release 1, we identified several regions with high $T_{\rm d}$, indicating localized heating by stars. We refilled these areas in the R, τ_{353}, and $T_{\rm d}$ maps with the average of the peripheral pixels: values in a circular region of radius r_1 are filled with the average of the pixels in an annulus with inner radius r_1 and outer radius r_2. For each region, the central position (l, b), r_1, and r_2 are summarized in Table 6. Since the area of high $T_{\rm d}$ located near

Table 6
Infrared Sources Excised and Interpolated Across in the Planck Dust Maps

Position		r_1	r_2	Object Name
l (deg)	b (deg)	(deg)	(deg)	
79.61	−30.25	0.12	0.15	
82.85	−50.65	0.12	0.15	
83.10	−45.46	0.12	0.15	
86.30	−38.20	0.60	0.65	3C 454.3 (Active galactic nucleus)
87.46	−29.73	0.12	0.15	NGC 7339 (Radio galaxy)
87.57	−39.12	0.12	0.15	
93.53	−40.35	0.12	0.15	RAFGL 3068 (Variable star)
93.91	−40.47	0.12	0.15	NGC 7625 (Interacting galaxies)
97.29	−32.52	0.12	0.15	IC 5298 (Seyfert2 galaxy)
98.88	−36.55	0.12	0.15	NGC 7678 (Active galactic nucleus)
104.26	−40.58	0.12	0.15	
104.46	−40.14	0.12	0.15	
111.37	−36.00	0.12	0.15	

Table 7
Parameters Ranges

Parameter	Range
Proton normalization	22.5–27.5
α_1	2.7–3.0
α_2	2.2–2.7
α_3	<0
$R_{\rm br1}$ (GV)	2–10
$R_{\rm br2}$ (GV)	0.1–2
δ_1	0.05–2
δ_2	0.05–2
ϕ	(0.85–1.15) × ϕ_0

Note. Normalization is the flux [c s^{-1} m^{-2} sr^{-1} (GeV/n)$^{-1}$] at $p = 10$ GeV. CR protons and He are assumed to share the value of the high-energy spectral break in rigidity. Therefore breaks in rigidity ($R_{\rm br}$) are given instead of breaks in momentum. ϕ_0 is the reference value of ϕ calculated based on Usoskin et al. (2017) and the observational period.

3C 454.3 is large, we used a larger radius for it. We found that the Planck Data Release 2 maps are less affected by infrared sources, and we had to mask only RAFGL 3068.

Appendix B
IC Model

We employed the recent work by Porter et al. (2017) to construct the IC model template. They employed 3D spatial models for the CR source distribution and the ISRF. They considered three different spatial distributions for the CR sources (differentiated by the ratio of the smooth-disk component to the spiral-arm component) and three ISRFs. The three CR source distributions are labeled SA0, SA50, and SA100; SA0 corresponds to a 100% (2D) disk, and SA100 corresponds to a 100% spiral-arm contribution. For the ISRF, they used a standard 2D ISRF (labeled Std) and two 3D ISRFs (labeled R12 and F98). We tested all nine IC models and a model used by Mizuno et al. (2016; labeled 54_77Xvarh7S) against the γ-ray data using our baseline gas model. We found that the SA0 models give a better fit than the others in terms of log-likelihoods, and that the differences among the three ISRF are minor. We therefore decided to use the SA0-Std model in this study.

Appendix C
CR and Gamma-Ray Fitting Framework

To investigate the interstellar CR spectrum in detail, we have developed a framework that simultaneously fits the CR and γ-ray data. It models the LIS and the solar-modulation effect using analytical formulae, and it uses a MCMC technique to constrain the model parameters. Specifically, we use the emcee[22] (Foreman-Mackey et al. 2013) python package that implements the affine-invariant ensemble sampler (Goodman & Weare 2010). Solar modulation is taken into account using a force-field approximation (Gleeson & Axford 1968), and the LIS is modeled as a power law of momentum with two breaks [see Equation (6)]. In the γ-ray spectrum calculation, we take account of p-p, p-He, He-p, and He-He interactions individually using the AAfrag package (Kachelriess et al. 2019) and the parameterizations of Kamae et al. (2006). Specifically, we adopt the calculations using the AAfrag package above 10 GeV/n and use the parameterizations of Kamae et al. (2006) below that energy. For the p-p interaction, we use the non-diffractive component of Kamae et al. (2006), since it smoothly connects to the AAfrag calculations. For the p-He and He-p interactions, we use the p-p interaction model of Kamae et al. (2006) multiplied by a factor of 4 to connect it smoothly to the AAfrag calculations. For the He-He interaction, we adopt a scale factor of 14. The contribution of heavier nuclei to the γ-ray spectrum is small, and we use an enhancement factor based on the formalism of Kachelriess et al. (2014) to scale the flux up to account for all other elements in the CRs and the interstellar gas. We adopt the spectra from Honda et al. (2004) and the abundances in the ISM from Meyer (1985) for the heavier nuclei in the CRs and the ISM gas, respectively. We also add an electron/positron bremsstrahlung model by Orlando (2018), specifically their best propagation model called PDDE. In that work, constraints on the electron/positron LIS were obtained by fitting CR direct measurements (Voyager 1 and AMS-02), local synchrotron emission from radio to microwaves (radio surveys and Planck data), and the emissivity of local γ-rays by Casandjian (2015). This method allows us to obtain a consistent electron/positron LIS independent from assumptions on the solar modulation.

The framework reads the AMS-02 data (taken in 2011–2013), the Voyager 1 data (taken in 2012), and the Fermi-LAT γ-ray data. To disentangle a possible degeneracy between the shape of the LIS and solar modulation, we can use other CR data. All the CR data are retrieved from the Cosmic-Ray Data Base (Maurin et al. 2014), but data points above 300 GeV are not used in the fitting. The CR data and γ-ray data share the same spectral shape of the LIS, but the normalizations (relative to that of AMS-02) are allowed to vary to account for possible systematic uncertainties. The solar-modulation potential ϕ is also set free for each CR data set, and it is set to be 0 V for the Voyager 1 data. The proton and He data of the same experiment and observational period share a common value of ϕ. Since the high-energy break is presumably due to a break in the interstellar diffusion coefficient, CR protons and He ions share δ_1 and a common value of rigidity for $p_{\rm br1}$. α_2 is also common among them. We also limit the parameter ranges as summarized in Table 7. Except for Voyager 1, ϕ is limited within ±15% of the value calculated based on Usoskin et al. (2017) and the observational period. For prior probabilities, we adopt a Gaussian distribution for LIS normalizations (relative

[22] https://emcee.readthedocs.io/en/stable/

Table 8
Data sets and Their ϕ and Relative Normalization

Experiment	ϕ (GV)	Relative normalization
AMS-02, 2011/05-2013/11 (proton, He)	614.7 ± 4.7	1
Voyager 1, 2012/10-2012/12 (proton, He)	0	1
AMS-01, 1998/06 (proton)	472[a]	1.028 ± 0.009
BESS-PolarI, 2004/12 (proton, He)	668.4 ± 4.4	1.012 ± 0.004
BESS-PolarII, 2007/12-2008/01 (proton, He)	386.5 ± 3.7	0.959 ± 0.004
BESS-TeV, 2002/08 (proton, He)	1055.0 ± 7.5	0.986 ± 0.004
PAMELA, 2006/07 (proton)	504.1 ± 5.0	1
PAMELA, 2008/03-2008/04 (proton)	404.6 ± 4.8	1
PAMELA, 2010/01 (proton)	293.7 ± 5.4	1
γ-ray emissivity, this work	0	1.066 ± 0.025

Note. The value of ϕ is set to 0 for the Voyager 1 data. LIS normalizations are scaled to that of AMS-02 and are allowed to vary. Some experiments do not have enough high-energy data points to constrain the normalization; in such a case, the relative normalization is fixed to 1.
[a] Although the best-fit value of ϕ is at the parameter limit, the spectrum is represented by the model well.

to that of AMS-02); the standard deviations are 0.05 and 0.1 for the CR data and γ-ray emissivity, respectively. We adopt a flat distribution for other parameters. The likelihood is calculated assuming a Gaussian distribution for each CR/γ-ray data points (the statistical error and systematic error are summed in quadrature). The framework then runs the MCMC fitting to constrain the LIS parameters and ϕ. The list of data sets used for this study and obtained values of ϕ and LIS normalization are summarized in Table 8.

ORCID iDs

T. Mizuno https://orcid.org/0000-0001-7263-0296
K. Hayashi https://orcid.org/0000-0001-6922-6583
I. V. Moskalenko https://orcid.org/0000-0001-6141-458X

References

Abdo, A. A., Ackermann, M., Ajello, M., et al. 2009a, Aph, 32, 193
Abdo, A. A., Ackermann, M., Ajello, M., et al. 2009b, ApJ, 703, 1249
Abdo, A. A., Ackermann, M., Ajello, M., et al. 2010, ApJ, 710, 133
Abdollahi, S., Acero, F., Ackermann, M., et al. 2020, ApJS, 247, 33
Ackermann, M., Ajello, M., Baldini, L., et al. 2011, ApJ, 726, 81
Ackermann, M., Ajello, M., Atwood, W. B., et al. 2012a, ApJ, 750, 3
Ackermann, M., Ajello, M., Allafort, A., et al. 2012b, ApJ, 755, 22
Atwood, W. B., Abdo, A. A., Ackermann, M., et al. 2009, ApJ, 697, 1071
Atwood, W. B., Albert, L., Baldini, L., et al. 2013, arXiv:1303.3514
Boschini, M. J., Torre, S. D., Gervasi, M., et al. 2020, ApJS, 250, 27
Bruel, P., Burnett, T. H., Digel, S. W., et al. 2018, arXiv:1810.11394
Casandjian, J.-M. 2015, ApJ, 806, 240
Cummings, A. C., Stone, E. C., Heikkila, B. C., et al. 2016, ApJ, 831, 18
Dame, T. M., Hartmann, D., & Thaddeus, P. 2001, ApJ, 547, 792
Dame, T. M. 2011, arXiv:1101.1499
Däppen, W. 2000, in Allen's Astrophysical Quantities, ed. A. N. Cox (4th edn.; New York: Springer), 27
Dickey, J. M., & Lockman, F. J. 1990, ARA&A, 28, 215
Ferriere, K. M. 2001, RvMP, 73, 1031
Fukui, Y., Okamoto, R., Kaji, R., et al. 2014, ApJ, 796, 59
Foreman-Mackey, D. W., Hogg, D., Lang, D., et al. 2013, PASP, 125, 306
Fukui, Y., Torii, K., Onishi, T., et al. 2015, ApJ, 798, 6
Fukui, Y., Koga, M., Maruyama, S., et al. 2021, PASJ, 73, S117
Górski, K. M., Hivon, E., Banday, A. J., et al. 2005, ApJ, 622, 759
Gleeson, J. J., & Axford, W. I. 1968, ApJ, 154, 1011
Goodman, J., & Weare, J. 2010, Comm. App Math. Comp. Sci., 5, 65
Grenier, I. A., Casandjian, J.-M., & Terrier, R. 2005, Sci, 307, 1292
Grenier, I. A., Black, J. H., & Strong, A. W. 2015, ARA&A, 53, 199
Hayashi, K., Mizuno, T., Fukui, Y., et al. 2019, ApJ, 884, 130
Honda, M., Kajita, T., Kasahara, K., et al. 2004, PhRvD, 70, 043008
HI4PI Collaboration 2016, A&A, 594, 116
Kachelriess, M., Moskalenko, I. V., & Ostapchenko, S. 2014, ApJ, 789, 136
Kachelriess, M., Moskalenko, I. V., & Ostapchenko, S. 2019, CoPhC, 245, 106846
Kalberla, P. M. W., & Kerp, J. 2009, ARA&A, 47, 27
Kalberla, P. M. W., & Haud, U. 2018, A&A, 619, 58
Kalberla, P. M. W., Kerp, J., & Haud, U. 2020, A&A, 639, 26
Kamae, T., Karlsson, N., Mizuno, T., et al. 2006, ApJ, 647, 692
Mattox, J. R., Bertsch, D. L., Chiang, J., et al. 1996, ApJ, 461, 396
Maurin, D., Melot, F., & Taillet, R. 2014, A&A, 569, 32
Meyer, J. P. 1985, ApJS, 57, 173
Mizuno, T., Abdollahi, S., Fukui, Y., et al. 2016, ApJ, 833, 278
Mizuno, T., Abdollahi, S., Fukui, Y., et al. 2020, ApJ, 890, 120
Moskalenko, I. V., Porter, T., & Strong, W. 2006, ApJL, 640, 155
Murray, C. M., Peek, J. E. G., Lee, M.-Y., et al. 2018, ApJ, 862, 131
Orlando, E. 2018, MNRAS, 475, 2724
Planck Collaboration XIX 2011, A&A, 536, 19
Planck Collaboration XI 2014, A&A, 571, 11
Planck Collaboration XXVIII 2015, A&A, 582, 31
Porter, T. A., Jóhannesson, G., & Moskalenko, I. V. 2017, ApJ, 846, 23
Ptuskin, V. S., Moskalenko, I. V., Jones, F. C., et al. 2006, ApJ, 642, 902
Reach, W. T., Bon-Chul, K., & Carl, H. 1994, ApJ, 429, 672
Remy, Q., Grenier, I. A., Marshall, D. J., & Casandjian, J. M. 2017, A&A, 601, 78
Remy, Q., Grenier, I. A., Marshall, D. J., & Casandjian, J. M. 2018, A&A, 611, 51
Schlegel, D. J., Finkbeiner, D. P., & Davis, M. 1998, ApJ, 500, 525
Smith, R. J., Glover, S. C. O., & Clark, P. C. 2004, MNRAS, 441, 1628
Strong, A. W., & Moskalenko, I. 1998, ApJ, 509, 212
Strong, A. W., Moskalenko, I. V., & Ptuskin, V. S. 2007, ARNPS, 57, 285
Strong, A. W. 2015, ICRC (The Hague), 34, 506
Usoskin, I. G., Agnieszka, G., Kovaltsov, G. A., et al. 2017, JGRA, 122, 3875
Wakker, B. P. 2001, ApJS, 136, 463
Welty, D. E., Hobbs, L. M., & Penprase, B. E. 1989, ApJ, 346, 232
Wolfire, M. G., Hollenbach, D., & McKee, C. F. 2010, ApJ, 716, 1191
Yamamoto, H., Kawamura, A., Tachihara, K., et al. 2006, ApJ, 642, 307